

Quantum-Inspired Algorithms beyond Unitary Circuits: the Laplace Transform

Noufal Jaseem,^{1,2} Sergi Ramos-Calderer,² Gauthameshwar S.,^{1,2}
Dingzu Wang,^{1,2} José Ignacio Latorre,² and Dario Poletti^{1,3,2,*}

¹*Science, Mathematics and Technology Cluster, Singapore University
of Technology and Design, 8 Somapah Road, 487372 Singapore*

²*Centre for Quantum Technologies, National University of Singapore 117543, Singapore*

³*Engineering Product Development Pillar, Singapore University of Technology and Design, 8 Somapah Road, 487372 Singapore*

(Dated: March 19, 2026)

Quantum-inspired algorithms can deliver substantial speedups over classical state-of-the-art methods by executing quantum algorithms with tensor networks on conventional hardware. Unlike circuit models restricted to unitary gates, tensor networks naturally accommodate non-unitary maps. This flexibility lets us design quantum-inspired methods that start from a quantum algorithmic structure, yet go beyond unitarity to achieve speedups. Here we introduce a tensor-network approach to compute the discrete Laplace transform, a non-unitary, aperiodic transform (in contrast to the Fourier transform). We encode a length- N signal on two paired n -qubit registers and decompose the overall map into a non-unitary exponential Damping Transform followed by a Quantum Fourier Transform, both compressed in a single matrix-product operator. This decomposition admits strong MPO compression to low bond dimension resulting in significant acceleration. We demonstrate simulations up to $N = 2^{30}$ input data points, with up to 2^{60} output data points, and quantify how bond dimension controls runtime and accuracy, including precise and efficient inference of pole locations.

Introduction — Quantum algorithms have attracted significant attention in the past few decades as they can lead to exponential or polynomial speedup for certain computations [1–4]. However, their implementation requires fault tolerant quantum computation which is still out of reach of current technologies, and some applications lack a method of efficiently loading the data on the quantum processor [5–9]. At the same time, up to certain sizes, it is possible to implement efficient simulations of some of these quantum algorithms, producing novel algorithms which run on classical machines [10–15].

These are known as *quantum-inspired* solutions, and while their realm of applicability is not as general as quantum algorithms, they provide faster algorithms in a relevant subset of cases. An important example of this strategy is the tensor-network implementation of the quantum Fourier transform [12, 15], that results in an acceleration over the fast Fourier transform on data efficiently compressible into tensor trains.

The Fourier transform is a unitary transformation, ubiquitous in signal processing, that can be translated to an efficient quantum algorithm, as its periodic structure gives rise to an exponential speedup. However, mathematics has gifted us with other functional transforms that do not have a straightforward quantum analogue, including the Laplace transform. The Laplace transform is an extension of the Fourier transform to complex-valued frequencies, and is nowadays commonly used to solve linear differential equations [16]. The discretized Laplace transform, also known as z -transform, is an important tool in signal processing, as it provides a complex-plane view of discrete signals, revealing stability, resonances,

and decay properties. It has applications in digital filter design, systems’ control, stability analysis etc. [17–20]. On the real positive axis, fast algorithms for the z -transform of a data-set of N inputs evaluated at M outputs achieve near-linear complexity $O(N + M)$ [21–23]. More generally, when evaluating along a specific contour in the complex plane, the z -transform can be implemented via the chirp- z approach with a computational cost of $O((N + M) \log(N + M))$ [17, 18], while on a dense 2D grid of possible outputs, with e.g. $M = N^2$, one would have a typical scaling of $O(NM)$.

Crucially, the z -transform is not unitary, nor has the periodic properties of the Fourier transform. Hence, a direct extension of the z -transform to a quantum algorithm is not possible. However, we highlight that potential quantum algorithms have been recently put forward [24, 25], based on block encoding the non-unitary transformation as a larger unitary operation. Tensor networks, though, are not limited to unitary operations. One can thus consider a class of quantum-inspired algorithms which, while being inspired by quantum algorithms, use operations beyond those available on a quantum processor.

In this letter, we develop a new class of *quantum-inspired* algorithms which, while building on quantum algorithms, they are assembled with non-unitary gates compressed into tensor networks. We thus formulate the z -transform ($\hat{z}\mathbb{T}$) as a low-bond-dimension tensor network acting on data encoded on a paired configuration of two registers $|j\rangle|j\rangle$. That is, only states $|j\rangle|j'\rangle$ with $j = j'$ are supported. The key observation is that on a polar grid $z_{k,\ell} = r_k e^{i\theta_\ell}$, each sample weight in the z -transform factors as $z_{k,\ell}^j = r_k^j e^{ij\theta_\ell}$, letting the radial and angular j -dependencies be realized on separate registers. This motivates a matrix-product-operator (MPO) realization composed of two main parts: a non-unitary

* dario_poletti@sutd.edu.sg

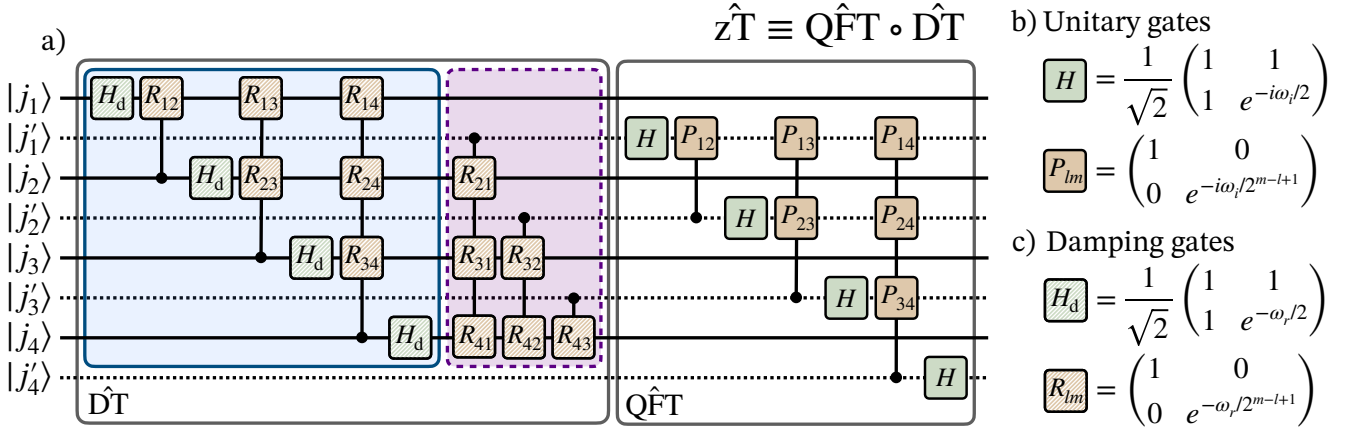


FIG. 1. (a) Decomposition of the z -transform into the damping transform $\hat{D}\hat{T}$, and the quantum Fourier transform $\hat{Q}\hat{F}\hat{T}$, shown in the paired-register layout $|j\rangle|j'\rangle$. The $\hat{D}\hat{T}$ consists of damping operations, defined in (c), separated into two steps. The solid blue box are damping operations acting on register $|j\rangle$, while the dashed purple box acts on both $|j\rangle|j'\rangle$, using register $|j'\rangle$ as controls. The $\hat{Q}\hat{F}\hat{T}$ acts only on register $|j'\rangle$ and uses unitary gates shown in (b). The controlled operations can be understood as sequential applications of controlled quantum gates, or as a joint MPO where identity operations are applied on wire crossings.

Damping Transform ($\hat{D}\hat{T}$) implementing the radial factors r_k^j , and a *Quantum Fourier Transform* ($\hat{Q}\hat{F}\hat{T}$) implementing the phases $e^{ij\theta_\ell}$. The resulting $\hat{z}\hat{T}$ pipeline produces the z -plane samples with modest, slowly growing MPO bond dimensions. This enables faster than $O(M \log M)$ runtime to generate a dense grid of $M = 2^m$ points from an $N = 2^n$ -sample input, where n is the number of qubits in a single register and $m = 2n$. We exemplify this scalable computation for data sizes up to $N = 2^{30}$ inputs and $M = 2^{60}$ outputs. We also introduce a practical workflow for inferring pole locations from dense z -plane samples, with an adjustable resolution. All of the results shown here have been performed simply on a laptop.

The z -transform — The z -transform of a finite sequence $\{x_j\}_{j=0}^{N-1}$ is

$$\chi(z) = \sum_{j=0}^{N-1} x_j z^j, \quad z = e^{-s}, \quad (1)$$

where $s = \sigma + i\omega$ is the logarithmic coordinate on the z -plane ($\sigma = -\log|z|$, $\omega = -\arg z$), and i is the imaginary unit. We evaluate χ on the grid $s_{k,\ell} = (\omega_r k + i\omega_i \ell)/N$, $k, \ell = 0, \dots, N-1$, so that the real scales ω_r and ω_i set, respectively, the radial (damped) and angular (oscillatory) resolution and, simultaneously, the accessible region via $|z| = e^{-\omega_r k/N}$ and $\arg z = -\omega_i \ell/N$. The corresponding outputs of the transform are thus

$$\chi_{k,\ell} = \sum_{j=0}^{N-1} x_j e^{-(\omega_r k/N)j} e^{-i(\omega_i \ell/N)j}. \quad (2)$$

Setting $\omega_r = 0$ restricts to the unit circle (pure spectral content); $\omega_r > 0$ shifts sampling inward ($|z| < 1$), while

$\omega_r < 0$ shifts it outward ($|z| > 1$). Throughout, we focus on $|z| \leq 1$, where the weighted terms decay with j , yielding numerically well-conditioned evaluations.

Quantum-Inspired Representation — We encode a length- $N = 2^n$ signal on two *paired* n -qubit registers in a copy layout,

$$|x\rangle = \sum_{j=0}^{N-1} x_j |j\rangle|j\rangle, \quad |j\rangle = |j_1 j_2 \dots j_n\rangle. \quad (3)$$

Then, the (generally non-unitary) linear z -transform is the map $|x\rangle \mapsto \sum_{k,\ell} \chi_{k,\ell} |k\rangle|\ell\rangle$. Equivalently, as an operator acting on the two registers,

$$\hat{z}\hat{T} = \frac{1}{N} \sum_{j,k,\ell=0}^{N-1} e^{-(\omega_r k/N)j} e^{-i(\omega_i \ell/N)j} |k\rangle|\ell\rangle \langle j|, \quad (4)$$

where the $1/N$ in front of the sum is a rescaling factor. We implement $\hat{z}\hat{T}$ by a two-stage decomposition

$$\hat{z}\hat{T} \equiv \hat{Q}\hat{F}\hat{T} \circ \hat{D}\hat{T}, \quad (5)$$

where $\hat{D}\hat{T}$ acts on register-1 with register-2 serving as a passive copy for control, and $\hat{Q}\hat{F}\hat{T}$ acts on register-2. A schematic of this two-stage decomposition is depicted in Fig. 1(a). On computational basis states, it yields

$$\hat{D}\hat{T} |j\rangle|j'\rangle = \frac{1}{\sqrt{N}} \sum_{k=0}^{N-1} e^{-(\omega_r k/N)j} |k\rangle|j'\rangle, \quad (6)$$

$$\hat{Q}\hat{F}\hat{T} |k\rangle|j'\rangle = \frac{1}{\sqrt{N}} \sum_{\ell=0}^{N-1} e^{-i(\omega_i \ell/N)j'} |k\rangle|\ell\rangle. \quad (7)$$

Non-unitary gates and damping transform — The tensor network implementation of the quantum Fourier

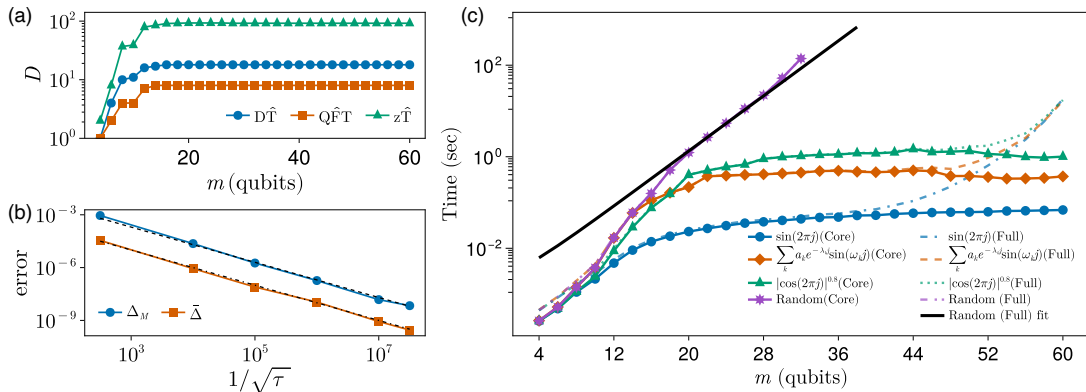


FIG. 2. **Numerical results for the MPO representation of the z -Transform.** a) Maximum MPO bond dimension D for $\hat{D}\hat{T}$, $\hat{Q}\hat{F}\hat{T}$, and the composite $z\hat{T}$ versus the number of output qubits $m = 2n = 2 \log_2(N)$ at cutoff 10^{-15} and $(\omega_r, \omega_i) = (2\pi, 2\pi)$, indicating strong MPO compressibility. N is the size of input data and n is the number of input qubits. b) Error versus the inverse square root of the SVD cutoff, $1/\sqrt{\tau}$, on log-log axes for $m = 20$ with a Gaussian random input $x_j \sim \mathcal{N}(0, 1)$. Max and mean absolute errors, Δ_M and $\bar{\Delta}$ respectively, exhibit $\sqrt{\tau}$ scaling as confirmed by linear fits (dashed/dot-dashed). c) End-to-end runtime (t) of the MPO z -transform ($\tau = 10^{-15}$) versus system size n (log-scale y -axis). “Full” includes the time required for encoding the signal into the initial MPS; “Core” does not include that cost. Curves for several input types are shown (see legend and Appendix D). For the *random* input, a tail fit of the “Full” timings (solid black) indicates runtime growing approximately linearly with $N = 2^n$; the fitted relation is $t \sim 1.3 \times 10^{-3} N + 10^{-3}$.

transform has been described in detail in [12]. Therefore, we focus here on the non-unitary gates used in the damping transform. We write $k = \sum_{\ell=1}^n k_\ell 2^{n-\ell}$ with $k_\ell \in \{0, 1\}$, and thus, for a given j , we get $\sum_{k=0}^{N-1} e^{-\omega_r k} e^{i j/N} |k\rangle = \bigotimes_{\ell=1}^n \left(|0\rangle + e^{-\omega_r j 2^{-\ell}} |1\rangle \right)$, which motivates defining a local “damping-Hadamard” gate

$$\mathcal{H}_{\text{damp}} = \frac{1}{\sqrt{2}} \begin{pmatrix} 1 & 1 \\ 1 & e^{-\omega_r/2} \end{pmatrix}, \quad (8)$$

where the prefactor $1/\sqrt{2}$ is only used as analogy with the Hadamard gate. Similarly, we also define “controlled-damping” gates which, for target qubit ℓ and control qubit m , act as

$$R_{l,m} = \exp \left[-\theta_{l,m} |1\rangle\langle 1|_l \otimes |1\rangle\langle 1|_m \right], \quad (9)$$

where $\theta_{l,m} = \omega_r/2^{m-l+1}$. Importantly, unlike the controlled phases of the $\hat{Q}\hat{F}\hat{T}$ which only need $m > l$ due to the 2π periodicity, the real exponent lacks periodicity, so the $\hat{D}\hat{T}$ requires controls from *all* bits m , both $m > l$ and $m < l$. We thus encode the data on two registers where the information appears only on matched pairs $|j\rangle|j\rangle$, and the second register is used to implement the controls of the $\hat{D}\hat{T}$ for $m < l$. The depiction of the z -transform in Fig. 1 a) accommodates both a circuit and tensor network interpretation. In Fig. 1 b) and c), the unitary and damping gates used in the graphical representation of the $\hat{Q}\hat{F}\hat{T}$ and $\hat{D}\hat{T}$ are defined. As a circuit, the controlled phase and damping gates are performed sequentially, while as a tensor network they can be merged

together as a single unit. In this representation the horizontal lines correspond to physical indices, while the vertical ones are auxiliary legs whose size is given by the bond dimension. In this graphical representation, we understand a crossing between a horizontal and a vertical line as acting with an identity operation on that qubit. Importantly, to reduce the bond dimension required to represent the data as a matrix product state, we order the qubits by alternating those from each register. In summary, the algorithm is initialized with a matrix product state representation of the $N = 2^n$ sized data encoded on matching pairs $|j\rangle|j\rangle$, then the matrix product operator corresponding to the z -transform is applied. At last, a SWAP operation is performed, as done for the $\hat{Q}\hat{F}\hat{T}$ algorithm. From one register, one obtains information on the amplitude part of the transform, and from the other register one acquires the information about the phase. A detailed, step-by-step description of this algorithm can be found in Appendices A and B, while the steps used to obtain a single, highly compressed, MPO from the circuit representation see App. C.

Results — Here we analyze the performance of this quantum-inspired strategy to perform the z -transform. Figure 2 a) shows the maximum MPO bond dimension reached for the $\hat{D}\hat{T}$, the $\hat{Q}\hat{F}\hat{T}$, and their composition $z\hat{T} = \hat{Q}\hat{F}\hat{T} \circ \hat{D}\hat{T}$, evaluated at a fixed relative SVD cutoff $\tau = 10^{-15}$. While it has been shown that the $\hat{Q}\hat{F}\hat{T}$ can be represented efficiently (excluding the final SWAP operation) as an MPO in [12], here we see that the bond dimension for the $\hat{D}\hat{T}$ is also under control. Furthermore,

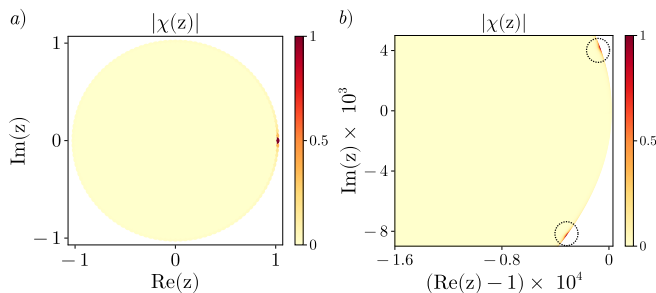


FIG. 3. Pole-location inference from the compressed MPS at $n = 20$, accessing 2^{40} candidate samples without materializing the full grid. Color encodes normalized $|\chi|$ ($|\chi|/\max|\chi|$). Each sample is computed on a (k, ℓ) grid point and plotted at the corresponding z -plane location $z_{k, \ell} = e^{-s_{k, \ell}}$. (a) $|\chi(z)|$ on a coarse $(k\ell)$ grid (step size 2^{12} ; 256×256 samples), with the MPO defined by $\omega_r = \omega_i = 2\pi$, reveals a peak near $z \approx 1$. (b) A fine scan, carried out with a different MPO using $\omega_r = 0.5$, $\omega_i = 2\pi$ for improved radial resolution, centered at $z = 1$ resolves two peaks at $z \approx 0.99997 + 0.00409i$ and $z \approx 0.99994 - 0.00817i$. Across the plotted samples, the max absolute error, $\Delta_M \lesssim 10^{-7}$. The extraction of the corresponding pole locations from the finite- N data is described in Appendix E.

the $\hat{z}\hat{T}$ can be compressed to a bond dimension smaller than the product of the $\hat{Q}\hat{F}\hat{T}$ and $\hat{D}\hat{T}$'s MPOs.

With an MPO representation of the z -transform, we can choose a different relative cut-off point τ for the singular values which affect the accuracy of the z -transform. To do so, we consider a signal of length $N = 2^{10}$ with x_j drawn independently from a zero-mean, unit-variance Gaussian ($x_j \sim \mathcal{N}(0, 1)$), so that the transform can be readily computed exactly. We calculate an input- ℓ_1 -normalized per-sample absolute error $\Delta_{k, \ell} = |(\tilde{\chi}_{k, \ell} - \chi_{k, \ell})| / \sum_{j=0}^{N-1} |x_j|$, with $\tilde{\chi}_{k, \ell} := N \langle k, \ell | \hat{z}\hat{T} | x \rangle$, where $\chi_{k, \ell}$ denotes the analytical value (Eq. 2), and $\tilde{\chi}_{k, \ell}$ is obtained from the MPO $\hat{z}\hat{T}$ compressed with relative cut-off τ . We report the mean, $\bar{\Delta}$ and maximum, Δ_M of $\Delta_{k, \ell}$ over the sampled (k, ℓ) grid. Figure 2b) shows both metrics versus τ . From numerical fits, both errors scale approximately as $\sqrt{\tau}$, with $\Delta_M \approx 0.2\sqrt{\tau}$ and $\bar{\Delta} \approx 10^{-2}\sqrt{\tau}$.

We have established that the MPO representation of the z -transform is accurate. We now study its efficiency. Figure 2 c) shows end-to-end runtimes for different types of input data, depicted by different symbols. For each case, we show both the time needed to execute only the $\hat{z}\hat{T}$, referred to as *Core* and depicted by continuous lines, and the total runtime, including the additional time required to convert the data into a matrix product state, referred to as *Full* and depicted by dashed lines. The data MPS is generated using randomized SVD with a truncation error threshold of 10^{-15} . For input data, we use a single sinusoidal function (blue circles), a sum of 10 sinusoidal functions each with a different exponential decay (orange diamonds), the absolute value of a sinusoidal function (green triangles), and random numbers

from a normal distribution (purple stars). More details are given in Appendix D. The runtime for non-random data, benchmarked here up to $N = 2^{30}$, is bounded from above by that of random data, whose runtime up to $N = 2^{16}$ grows approximately linearly with N . Importantly, this transform provides $M = N^2$ outputs. This should be compared to the chirp- z transform (CZT), a standard method that is often evaluated on a spiral contour in the complex plane. This has a computational cost of $O((N+M)\log(N+M))$ stemming from two forward and one inverse FFT and $O(N+M)$ chirp multiplications [17, 18]. Our setting uses $M = N^2$, which yields a baseline computational cost of $O(M \log M) = O(N^2 \log N)$ to cover the $N \times N$ grid. Thus, an empirical linear scaling for the MPO approach is already advantageous relative to the implementation of the CZT transform for large N , especially for non-random inputs.

At this point, considering the large size of the output data, an important matter to tackle is the accessibility of the data. Thanks to the binary encoding of the data into an MPS, this data can be accessed at different levels of detail, allowing us to zoom into areas of interest. For example, we consider as input data the sequence $x_j \propto a^j \cos(\omega_0 j)$, whose z -transform for an infinite series has poles at $z = (1/a) e^{\pm i\omega_0} \approx 0.99984 + 0.00408i, 0.99981 - 0.00816i$, for $a = 1.00015e^{i0.002}$ and $\omega_0 = 0.0061$. In Fig. 3(a) we show the coarse-grained form of the z -transform, whereby we only consider the first 8 digits from the $\hat{D}\hat{T}$ and $\hat{Q}\hat{F}\hat{T}$ portions.

This shows that the z -transform has, at least, a pole close to the $z = 1$ point in the complex plane. The MPS representation allows us to zoom in to that portion of the complex plane and clearly single out the two inferred poles locations, as shown in Fig. 3(b), see Appendix E for more details. Alternatively, we can also use the autoregressive properties of the solution matrix product state to sample the node configurations. The same scanning strategy can also be applied to find zeros. An example is presented in Appendix E, where three closely spaced zeros are clearly resolved in the finite- N truncated transform as localized minima of $|X(z)|$.

Conclusions — We presented a quantum-inspired discrete Laplace transform, or z -transform, using MPOs with a decomposition into a damping transform and a quantum Fourier transform on a pair of registers. Our quantum-inspired tensor network implementation of the z -transform offers efficient computation for signals of large input size, and dense sampling in the z -plane. We represent the map $x_j \mapsto \chi_{k, \ell}$ as a compressed MPO acting on a signal encoded into a matrix-product state which returns a matrix product state over the output indices (k, ℓ) . This enables on-demand evaluation of dense polar grids and multiple contours without materializing the full array with M elements. Our numerical calculations indicate significant compression, efficient runtime, and reliable pole-location inference on large grids; the implementation is available as open-source code on GitHub [26]. This can lead to appli-

cations, for instance in the design of transmission functions, whose properties depend significantly on the location of their zeros and poles. More importantly, we have shown a tensor-network-based quantum-inspired computation that builds on non-unitary gates, thus providing an extension to this class of algorithms. This line of re-

search deserves further exploration in the future.

Acknowledgements. We acknowledge support from the Singapore Ministry of Education from grant MOE-T2EP50123-0017, and from the Centre for Quantum Technologies grant CQT_SUTD_2025_01. Constructing the z -transform MPO and related circuit tensors was performed using the software package ITensor [27] in Julia.

-
- [1] L. K. Grover, in *Proceedings of the twenty-eighth annual ACM symposium on Theory of computing* (1996) pp. 212–219.
- [2] S. Lloyd, *Science* **273**, 1073 (1996).
- [3] P. W. Shor, *SIAM review* **41**, 303 (1999).
- [4] A. Montanaro, *npj Quantum Information* **2**, 1 (2016).
- [5] J. Preskill, *Proceedings of the Royal Society of London. Series A: Mathematical, Physical and Engineering Sciences* **454**, 385 (1998).
- [6] A. G. Fowler, M. Mariantoni, J. M. Martinis, and A. N. Cleland, *Physical Review A—Atomic, Molecular, and Optical Physics* **86**, 032324 (2012).
- [7] J. Preskill, *Quantum* **2**, 79 (2018).
- [8] S. Aaronson, *Nature Physics* **11**, 291 (2015).
- [9] J. Biamonte, P. Wittek, N. Pancotti, P. Rebentrost, N. Wiebe, and S. Lloyd, *Nature* **549**, 195 (2017).
- [10] L. Ma and C. Yang, *Journal of Computational Science* **59**, 101561 (2022).
- [11] F. Pan and P. Zhang, *Physical Review Letters* **128**, 030501 (2022).
- [12] J. Chen, E. Stoudenmire, and S. R. White, *PRX Quantum* **4**, 040318 (2023).
- [13] F. Pan, H. Gu, L. Kuang, B. Liu, and P. Zhang, *ACM Transactions on Quantum Computing* **5**, 1 (2024).
- [14] A. De Girolamo, P. Facchi, P. Rabl, S. Pascazio, C. Lupo, and G. Magnifico, *Physical Review Research* **7**, 043170 (2025).
- [15] M. Niedermeier, J. L. Lado, and C. Flindt, *Physical Review Research* **6**, 033325 (2024).
- [16] M. H. Hayes, *Statistical digital signal processing and modeling* (John Wiley & Sons, 1996).
- [17] L. R. Rabiner, R. W. Schafer, and C. M. Rader, *Bell System Technical Journal* **48**, 1249 (1969).
- [18] A. V. Oppenheim, A. S. Willsky, and S. H. Nawab, *Signals and Systems*, 2nd ed. (Prentice Hall, 1997).
- [19] B. Bozkurt, B. Doval, C. d’Alessandro, and T. Dutoit, *IEEE signal processing letters* **12**, 344 (2005).
- [20] R. Tong and R. W. Cox, *Magnetic Resonance in Medicine: An Official Journal of the International Society for Magnetic Resonance in Medicine* **41**, 253 (1999).
- [21] V. Rokhlin, *Journal of Complexity* **4**, 12 (1988).
- [22] J. Strain, *mathematics of computation* **58**, 275 (1992).
- [23] Y. L. Loh, *Journal of Computational Mathematics and Data Science* **8**, 100082 (2023).
- [24] J. Zylberman, *Fast laplace transforms on quantum computers* (2024), arXiv:2412.05173 [quant-ph].
- [25] A. K. Singh, A. K. Patra, A. K. S. V., S. S. P., R. Bhat, and J. G., *A polylogarithmic-time quantum algorithm for the laplace transform* (2025), arXiv:2512.17980 [quant-ph].
- [26] QILaplace.jl: Quantum-inspired laplace transform, <https://github.com/SUTD-MDQS/QILaplace.jl> (2026),

gitHub repository, accessed 2026-01-07.

- [27] M. Fishman, S. White, and E. M. Stoudenmire, *SciPost Physics Codebases*, 004 (2022).

Appendix A: Damping Transform and example of implementation

Given that the application of tensor networks to implement the Quantum Fourier Transform (QFT) has been previously investigated by Chen, Stoudenmire, and White in their 2023 study [12], this work narrows its focus to the implementation of the real-exponential component. For each j , the transformation can be expressed as follows.

$$|j\rangle |j'\rangle \xrightarrow{\text{DT}} \frac{1}{\sqrt{2^n}} \sum_{k=0}^{2^n-1} \exp\left(\frac{-\omega_r k j}{2^n}\right) |k\rangle |j'\rangle. \quad (\text{A1})$$

Here, $|j'\rangle$ denotes the second register, an identical copy of $|j\rangle$, which is left unchanged by this step. Write k in binary as $k = k_1 2^{n-1} + k_2 2^{n-2} + \dots + k_n 2^0$ (where each $k_\ell \in \{0, 1\}$). Then

$$\begin{aligned} \sum_{k=0}^{2^n-1} e^{\frac{-\omega_r k j}{2^n}} |k\rangle &= \sum_{k_1=0}^1 \sum_{k_2=0}^1 \dots \sum_{k_n=0}^1 \exp\left[-\omega_r j (k_1 2^{n-1} \right. \\ &\quad \left. + k_2 2^{n-2} + \dots + k_n 2^0)\right] |k_1 k_2 \dots k_n\rangle \\ &= \sum_{k_1=0}^1 \dots \sum_{k_n=0}^1 \prod_{\ell=1}^n \exp\left(-\omega_r j k_\ell 2^{-\ell}\right) |k_1 k_2 \dots k_n\rangle. \end{aligned} \quad (\text{A2})$$

We can factorize the sum over each qubit index:

$$\begin{aligned} \Rightarrow & \frac{1}{\sqrt{2^n}} \sum_{k_1=0}^1 \dots \sum_{k_n=0}^1 \exp\left(-\omega_r j (k_1 2^{n-1} + \dots + k_n 2^0)\right) \\ & |k_1 \dots k_n\rangle |j'\rangle \\ &= \frac{1}{\sqrt{2^n}} (|0\rangle + e^{-\omega_r j 2^{n-1}} |1\rangle) (|0\rangle + e^{-\omega_r j 2^{n-2}} |1\rangle) \\ & \dots (|0\rangle + e^{-\omega_r j 2^0} |1\rangle) |j'\rangle. \end{aligned} \quad (\text{A3})$$

In the following, we show some details of how this can be implemented.

1. First Qubit

1. Start with the state $|j_1 j_2 \dots j_n\rangle |j'_1 \dots j'_n\rangle$.
2. Apply \mathcal{H}_1 to qubit 1 ($|j_1\rangle$):

$$|j_1\rangle \longrightarrow \frac{1}{\sqrt{2}} \left(|0\rangle + e^{-\omega_r j_1/2} |1\rangle \right). \quad (\text{A4})$$

This yields

$$\frac{1}{\sqrt{2}} \left(|0\rangle + e^{-\omega_r j_1/2} |1\rangle \right) |j_2 j_3 \dots j_n\rangle |j'_1 \dots j'_n\rangle.$$

3. Apply $R_{1,m}$ for $m = 2, \dots, n$: Each gate accumulates the contribution from the qubit m into the exponent for the first qubit's $|1\rangle$ component.

$$\begin{aligned} & \frac{1}{\sqrt{2}} \left(|0\rangle + e^{-\omega_r j_1/2} |1\rangle \right) |j_2 \dots j_n\rangle |j'_1 \dots j'_n\rangle \xrightarrow{R_{12}} \\ & \frac{1}{\sqrt{2}} \left(|0\rangle + e^{-\omega_r (j_1/2 + j_2/2^2)} |1\rangle \right) |j_2 \dots j_n\rangle |j'_1 \dots j'_n\rangle. \end{aligned} \quad (\text{A5})$$

After applying all these gates, the factor yields

$$\exp \left[-\omega_r \left(j_1 2^{-1} + j_2 2^{-2} + \dots + j_n 2^{-n} \right) \right] = \exp \left(-\omega_r \frac{j}{2^n} \right),$$

where $j = j_1 2^{n-1} + \dots + j_n 2^0$. Thus, the first qubit state transform to

$$\frac{1}{\sqrt{2}} \left(|0\rangle + e^{-\omega_r j/2^n} |1\rangle \right),$$

and the combined state becomes

$$\frac{1}{\sqrt{2}} \left(|0\rangle + e^{-\omega_r j/2^n} |1\rangle \right) |j_2 j_3 \dots j_n\rangle |j'_1 \dots j'_n\rangle.$$

2. Second Qubit

1. Next, apply \mathcal{H} to $|j_2\rangle$:

$$|j_2\rangle \longrightarrow \frac{1}{\sqrt{2}} \left(|0\rangle + e^{-\omega_r j_2/2} |1\rangle \right).$$

2. Apply $R_{2,m}$ for $m \neq 2$, i.e., $m = 1, 3, 4, \dots, n$. Unlike the QFT, which uses control qubits $m > 2$, the

damping transform requires controls from all other qubits, including $m = 1$, due to the real exponent. The second register's copy of the state preserves the original qubit states, ensuring correct phase accumulation despite prior gate operations on qubit 1. After these gates, the phase factor results in

$$\frac{1}{\sqrt{2}} \left(|0\rangle + e^{-\omega_r j/2^{n-1}} |1\rangle \right).$$

Thus, the state after transforming the first two qubits is

$$\begin{aligned} & \frac{1}{\sqrt{2}} \left(|0\rangle + e^{-\omega_r j/2^n} |1\rangle \right) \frac{1}{\sqrt{2}} \left(|0\rangle + e^{-\omega_r j/2^{n-1}} |1\rangle \right) \\ & |j_3 \dots j_n\rangle |j'_1 \dots j'_n\rangle \end{aligned} \quad (\text{A6})$$

3. Remaining Qubits

Repeat the same procedure for the remaining qubits $\ell = 3, 4, \dots, n$, each time applying the damping Hadamard gate \mathcal{H}_ℓ followed by the controlled damping gates $R_{\ell,m}$. The final state becomes

$$\begin{aligned} & \frac{1}{\sqrt{2}} \left(|0\rangle + e^{-\omega_r j/2^n} |1\rangle \right) \frac{1}{\sqrt{2}} \left(|0\rangle + e^{-\omega_r j/2^{n-1}} |1\rangle \right) \dots \\ & \frac{1}{\sqrt{2}} \left(|0\rangle + e^{-\omega_r j/2^1} |1\rangle \right) |j'_1 \dots j'_n\rangle \end{aligned} \quad (\text{A7})$$

Thus, the circuit implemented above prepares the quantum state corresponding to the $\hat{\text{DT}}$ transform as defined in Eq. (A3), but with the qubit order reversed, requiring a swap of qubits to match the specified ordering.

4. An Example of $\hat{\text{DT}}$ for $n = 3$

For $n = 3$, the Eq.(A1) yields,

$$|j\rangle |j'\rangle \longmapsto \frac{1}{\sqrt{2^3}} \sum_{k=0}^{2^3-1} \exp \left(\frac{-\omega_r k j}{2^3} \right) |k\rangle |j'\rangle. \quad (\text{A8})$$

Here, $|j'\rangle$ denotes the second register, an identical copy of $|j\rangle$, which is left unchanged by this step. Write k in binary as $k = k_1 2^2 + k_2 2^1 + k_3 2^0$ (where each $k_\ell \in \{0, 1\}$). Then

$$\begin{aligned}
\sum_{k=0}^{2^3-1} e^{-\frac{\omega_r k j}{2^3}} |k\rangle |j'\rangle &= \frac{1}{\sqrt{2^3}} \sum_{k_1=0}^1 \sum_{k_2=0}^1 \sum_{k_3=0}^1 \exp\left(-\omega_r j (k_1 2^{-1} + k_2 2^{-2} + k_3 2^{-3})\right) |k_1 k_2 k_3\rangle |j'_1 j'_2 j'_3\rangle \\
&= \frac{1}{\sqrt{2^3}} (|0\rangle + e^{-\omega_r j/2^1} |1\rangle) (|0\rangle + e^{-\omega_r j/2^2} |1\rangle) (|0\rangle + e^{-\omega_r j/2^3} |1\rangle) |j'_1 j'_2 j'_3\rangle. \quad (\text{A9})
\end{aligned}$$

We now verify that the DT circuit implements Eq.(A9).

Qubit 1:

$$\begin{aligned}
|j_1 j_2 j_3\rangle |j'_1 j'_2 j'_3\rangle &\xrightarrow{\mathcal{H}} \frac{1}{\sqrt{2}} (|0\rangle + e^{-\omega_r j_1/2} |1\rangle) |j_2 j_3\rangle |j'_1 j'_2 j'_3\rangle \xrightarrow{\mathcal{R}_{13}} \frac{1}{\sqrt{2}} (|0\rangle + e^{-\omega_r (j_1/2 + j_2/2^2)} |1\rangle) |j_2 j_3\rangle |j'_1 j'_2 j'_3\rangle \\
&\xrightarrow{\mathcal{R}_{13}} \frac{1}{\sqrt{2}} (|0\rangle + e^{-\omega_r (j_1/2 + j_2/2^2 + j_3/2^3)} |1\rangle) |j_2 j_3\rangle |j'_1 j'_2 j'_3\rangle = \frac{1}{\sqrt{2}} (|0\rangle + e^{-\omega_r j/2^3} |1\rangle) |j_2 j_3\rangle |j'_1 j'_2 j'_3\rangle
\end{aligned}$$

Qubit 2:

$$\begin{aligned}
\frac{1}{\sqrt{2}} (|0\rangle + e^{-\omega_r j/2^3} |1\rangle) |j_2 j_3\rangle |j'_1 j'_2 j'_3\rangle &\xrightarrow{\mathcal{H}} \frac{1}{\sqrt{2}} (|0\rangle + e^{-\omega_r j/2^3} |1\rangle) \frac{1}{\sqrt{2}} (|0\rangle + e^{-\omega_r j_2/2} |1\rangle) |j_3\rangle |j'_1 j'_2 j'_3\rangle \\
&\xrightarrow{\mathcal{R}_{23}} \frac{1}{\sqrt{2}} (|0\rangle + e^{-\omega_r j/2^3} |1\rangle) \frac{1}{\sqrt{2}} (|0\rangle + e^{-\omega_r (j_2/2 + j_3/2^2)} |1\rangle) |j_3\rangle |j'_1 j'_2 j'_3\rangle \\
&\xrightarrow{\mathcal{R}_{21'}} \frac{1}{\sqrt{2}} (|0\rangle + e^{-\omega_r j/2^3} |1\rangle) \frac{1}{\sqrt{2}} (|0\rangle + e^{-\omega_r (j_2/2 + j_3/2^2 + j'_1/2^0)} |1\rangle) |j_3\rangle |j'_1 j'_2 j'_3\rangle \\
&= \frac{1}{\sqrt{2}} (|0\rangle + e^{-\omega_r j/2^3} |1\rangle) \frac{1}{\sqrt{2}} (|0\rangle + e^{-\omega_r j/2^2} |1\rangle) |j_3\rangle |j'_1 j'_2 j'_3\rangle
\end{aligned}$$

We use $j'_1 = j_1$, as j'_1 is a copy of j_1 , to obtain the above equation.

Qubit 3:

$$\begin{aligned}
&\frac{1}{\sqrt{2}} (|0\rangle + e^{-\omega_r j/2^3} |1\rangle) \frac{1}{\sqrt{2}} (|0\rangle + e^{-\omega_r j/2^2} |1\rangle) |j_3\rangle |j'_1 j'_2 j'_3\rangle \\
&\xrightarrow{\mathcal{H}} \frac{1}{\sqrt{2}} (|0\rangle + e^{-\omega_r j/2^3} |1\rangle) \frac{1}{\sqrt{2}} (|0\rangle + e^{-\omega_r j/2^2} |1\rangle) \frac{1}{\sqrt{2}} (|0\rangle + e^{-\omega_r j_3/2} |1\rangle) |j'_1 j'_2 j'_3\rangle \\
&\xrightarrow{\mathcal{R}_{31'}} \frac{1}{\sqrt{2}} (|0\rangle + e^{-\omega_r j/2^3} |1\rangle) \frac{1}{\sqrt{2}} (|0\rangle + e^{-\omega_r j/2^2} |1\rangle) \frac{1}{\sqrt{2}} (|0\rangle + e^{-\omega_r (j_3/2 + j'_1/2^{-1})} |1\rangle) |j'_1 j'_2 j'_3\rangle \\
&\xrightarrow{\mathcal{R}_{32'}} \frac{1}{\sqrt{2}} (|0\rangle + e^{-\omega_r j/2^3} |1\rangle) \frac{1}{\sqrt{2}} (|0\rangle + e^{-\omega_r j/2^2} |1\rangle) \frac{1}{\sqrt{2}} (|0\rangle + e^{-\omega_r (j_3/2 + j'_1/2^{-1} + j'_2/2^0)} |1\rangle) |j'_1 j'_2 j'_3\rangle \\
&= \frac{1}{\sqrt{2}} (|0\rangle + e^{-\omega_r j/2^3} |1\rangle) \frac{1}{\sqrt{2}} (|0\rangle + e^{-\omega_r j/2^2} |1\rangle) \frac{1}{\sqrt{2}} (|0\rangle + e^{-\omega_r j/2} |1\rangle) |j'_1 j'_2 j'_3\rangle \quad (\text{A10})
\end{aligned}$$

which matches Eq.(A9) up to a swap of the qubit order.

Appendix B: Input state MPS

To prepare the input state MPS for the state (Eq. (3)),

$$|x\rangle = \sum_i d_i |i\rangle_A |i\rangle_B = \sum_{i_1, \dots, i_n} d_{i_1 \dots i_n} |i_1 \dots i_n\rangle_A |i_1 \dots i_n\rangle_B,$$

we first encode the data as

$$|\psi\rangle = \sum_{i=0}^{2^n-1} d_i |i\rangle = \sum_{i_1, \dots, i_n \in \{0,1\}} d_{i_1 \dots i_n} |i_1 \dots i_n\rangle,$$

The transformation is not unitary, but it is still linear. Since it implements the correct transformation on each element of the computational basis, it also performs it on its superpositions.

and, from its MPS, build the MPS for the resulting $2n$ -qubit state. If this $2n$ -qubit state is decomposed into an MPS in the order $(i_1, \dots, i_n, i'_1, \dots, i'_n)$, long-range A/B correlations drive exponential growth of the MPS bond dimension, negating any advantage of a z -transform using a compressed MPO. In contrast, the interleaved order $(i_1, i'_1, i_2, i'_2, \dots, i_n, i'_n)$ localizes the copy constraints δ_{i_k, i'_k} and keeps the MPS bond dimension small for *structured* signals (e.g., a few damped sinusoids), whereas generic random signals the bond dimension remain high. To avoid materializing the 2^{2n} tensor, we first build an n -qubit MPS for $|\psi\rangle$ and then *lift* it to $2n$ sites by inserting local copy tensors; this preserves compression, for example, $x_j = \sin(\omega_0 j)$ yields bond-dimension, $D = 2$ on n qubits and bond-dimension, $D \approx 4$ after lifting, making the subsequent $\hat{z}\hat{T}$ MPO application tractable.

Appendix C: Constructing the Matrix Product Operator

We follow the tensor-network reinterpretation of quantum circuits as matrix product operators, as used for the QFT in Ref. [12], and apply it to the non-unitary damping circuit underlying our z -transform. The circuit for DT is shown in Fig. C1. Below we show how each gate in Fig. C1 is mapped to a local tensor, so that the entire circuit can be written as a tensor network.

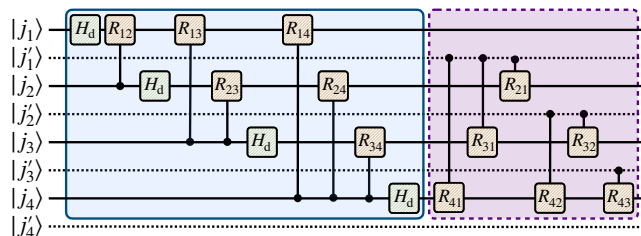


FIG. C1. Circuit diagram of the damping transform $\hat{D}\hat{T}$, which forms the non-unitary part of the z -transform $\hat{z}\hat{T}$. Each two-qubit controlled gate and the ‘‘damping-Hadamard’’ in this circuit will be mapped to a local tensor to obtain an MPO.

We start with the controlled damping gate

$$\begin{array}{c} \bullet \\ | \\ \text{---} \\ | \\ \boxed{R(\theta)} \\ | \\ \text{---} \end{array} = |0\rangle\langle 0| \otimes \mathbb{1} + |1\rangle\langle 1| \otimes R(\theta), \quad (\text{C1})$$

which applies the identity $\mathbb{1}$ to the data register if the control is $|0\rangle$ and applies a non-unitary map $R(\theta) = \text{diag}(1, e^{-\theta})$ if the control is $|1\rangle$. This two-qubit operator can be factored into an inner product of two operator-valued vectors,

$$|0\rangle\langle 0| \otimes \mathbb{1} + |1\rangle\langle 1| \otimes R(\theta) = (|0\rangle\langle 0| \quad |1\rangle\langle 1|) \begin{pmatrix} \mathbb{1} \\ R(\theta) \end{pmatrix}. \quad (\text{C2})$$

This factorization rewrites the controlled damping gate as the contraction of two order-3 tensors, i.e., as a two-site MPO. The first tensor is the copy tensor,

$$\begin{array}{c} | \\ \text{---} \\ | \\ \text{---} \end{array} = (|0\rangle\langle 0| \quad |1\rangle\langle 1|), \quad (\text{C3})$$

and the second is the damping tensor,

$$\begin{array}{c} | \\ \boxed{R(\theta)} \\ | \end{array} = \begin{pmatrix} \mathbb{1} \\ R(\theta) \end{pmatrix}. \quad (\text{C4})$$

The copy tensor maps the control branches $|0\rangle$ and $|1\rangle$ onto a virtual bond index, and the damping tensor applies either $\mathbb{1}$ or $R(\theta)$ conditioned on that index, so the control is carried by the MPO bond. Two such controlled-damping gates applied consecutively can be fused into a single MPO,

$$\begin{array}{c} \bullet \quad \bullet \\ | \quad | \\ \text{---} \quad \text{---} \\ | \quad | \\ \boxed{R(\theta_1)} \\ | \quad | \\ \text{---} \quad \text{---} \\ | \quad | \\ \boxed{R(\theta_2)} \\ | \quad | \\ \text{---} \quad \text{---} \end{array} = \begin{array}{c} \bullet \\ | \\ \text{---} \\ | \\ \boxed{R(\theta)} \\ | \\ \text{---} \\ | \\ \boxed{R(\theta_2)} \\ | \\ \text{---} \end{array} = \begin{array}{c} \bullet \\ | \\ \text{---} \\ | \\ \boxed{R(\theta)} \\ | \\ \text{---} \\ | \\ \boxed{R(\theta_2)} \\ | \\ \text{---} \end{array} \quad (\text{C5})$$

whose internal block is an order-4 tensor,

$$\begin{array}{c} \bullet \\ | \\ \text{---} \\ | \\ \boxed{R(\theta_1)} \\ | \\ \text{---} \\ | \\ \bullet \end{array} = \begin{array}{c} | \\ \text{---} \\ | \\ \text{---} \end{array} \begin{pmatrix} \mathbb{1} & 0 \\ 0 & R(\theta) \end{pmatrix}. \quad (\text{C6})$$

Similarly, multiple damping gates sharing a common control can be fused into a controlled multi-site MPO; we refer to this as the ‘controlled-damping MPO’.

In addition, the on-site ‘‘damping-Hadamard’’ tensor is given by

$$\begin{array}{c} \bullet \\ | \\ \text{---} \\ | \\ \boxed{H_d} \\ | \\ \text{---} \end{array} = \frac{1}{\sqrt{2}} \begin{pmatrix} 1 & 1 \\ 1 & e^{-\omega_r/2} \end{pmatrix}. \quad (\text{C7})$$

Using these tensor assignments, the damping circuit in Fig. C1 maps directly to the MPO/tensor-network representation built from the damped-Hadamard and controlled-damping MPOs shown in Fig. 1. We now outline the construction of the *truncated* $\hat{z}\hat{T}$ MPO for this network.

MPO contraction (zip-up / zip-down). We obtain the QFT MPO via the zip-up/zip-down scheme of Ref. [12]. For the damping network, we use a similar iterate-merge pattern with QR preconditioning before truncation.

A controlled-damping MPO is the multi-site MPO formed by fusing damping gates sharing a common control (Fig. 1). For two adjacent controlled-damping MPOs acting on the single-register branch $(|j\rangle)$: (i) locally contract the corresponding site tensors over physical indices; (ii) perform a bottom-to-top series of QR factorizations

to place the orthogonality center (OC) at site 1, writing $A = QR$, keeping Q on-site and pushing R upward—this canonizes the MPO; (iii) at the OC, take a truncated singular-value decomposition (SVD) $X = USV^\dagger$ with a relative cutoff, keeping V on-site and pushing US downward. Repeating the SVD/push cycle compresses and moves the OC to the bottom. The resulting MPO is then merged with the next controlled-damping MPO by the same steps. Iterating over all controlled-damping MPOs yields $\hat{D}\hat{T}$ on $|j\rangle$. We then repeat the same pairwise merge on the joint branch ($|j\rangle \otimes |j'\rangle$) to obtain the joint component; composing these two components gives the (single) $\hat{D}\hat{T}$ MPO. Finally, composing the $\hat{D}\hat{T}$ MPO with the $\hat{Q}\hat{F}\hat{T}$ MPO, with appropriate QR sweeps and truncated SVDs, produces a single, compressed MPO realizing the full z -transform.

The singular-value spectra σ_k of the MPO decompositions are shown in Fig. C2 for all internal bonds at $n = 30$ (\log_{10} y-axis). Figure C3 focuses on the bond with the largest dimension and shows the spectra for $n \in \{10, 20, 30\}$; exponential fits, plotted on the same \log_{10} scale, indicate an approximately exponential decay, $\sigma_k \propto e^{-\alpha k}$. This rapid decay explains the low bond dimensions observed for these MPOs and enables efficient simulations of the corresponding transforms.

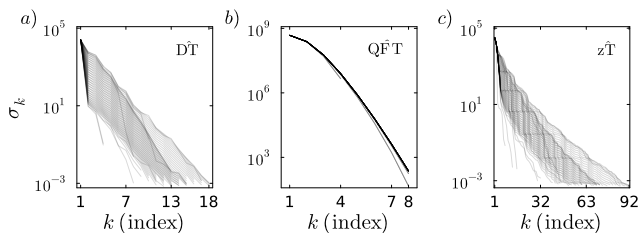


FIG. C2. Singular-value spectra across all internal bonds for $n = 30$. Panels (a), (b), and (c) show σ_k versus index k for $\hat{D}\hat{T}$, $\hat{Q}\hat{F}\hat{T}$, and $\hat{z}\hat{T}$, respectively, on a \log_{10} y-axis with relative cutoff $\tau = 10^{-15}$ and $(\omega_\tau, \omega_i) = (2\pi, 2\pi)$. Each curve corresponds to the spectrum at a single bond.

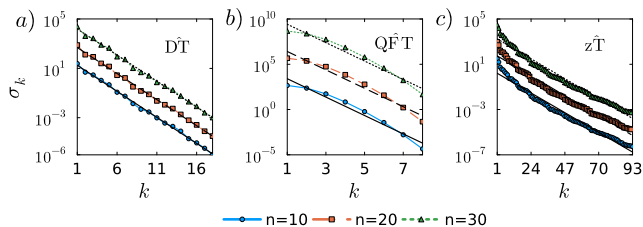


FIG. C3. Singular-value spectra at the first bond attaining the maximum bond dimension for $\hat{D}\hat{T}$ (a), $\hat{Q}\hat{F}\hat{T}$ (b), and $\hat{z}\hat{T}$ (c), for $n \in \{10, 20, 30\}$, are shown on a \log_{10} y-axis with relative cutoff $\tau = 10^{-15}$. Exponential fits of the form $\sigma_k = Ae^{-\alpha k}$ (black lines), plotted on the same \log_{10} scale, closely match the numerical data (markers), supporting an efficient low-rank MPO approximation.

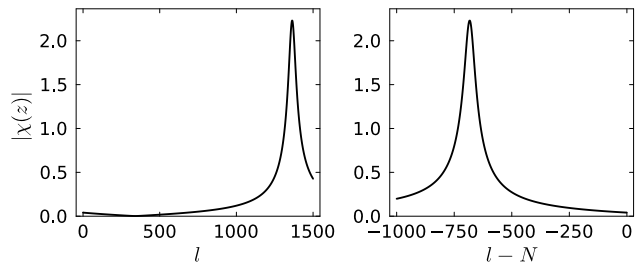


FIG. C4. Unit-circle ($k = 0$) angular slices in the two separated l regions. The dominant responses occur at $l = 1364$ and $l = 1047893$.

Appendix D: Input signals

For Fig. 2(c), we use signals of length $N = 2^n$ with samples indexed by $j = 0, \dots, N - 1$ and sampling interval $\Delta t = 5/2^n$. Random numbers are generated using Julia’s `MersenneTwister` pseudorandom generator (from the standard `Random` module) with fixed seeds to ensure exact reproducibility. The following signal families are used: (i) a pure sinusoid, $x[j] = \sin(2\pi j \Delta t)$; (ii) Gaussian noise, $x[j] \sim \mathcal{N}(0, 1)$ independently for all j , generated with seed 1234; (iii) a multi-sinusoid with exponential decay, $x[j] = \sum_{k=1}^{n_{\text{terms}}} a_k \sin(\omega_k \Delta t j) e^{\lambda_k \Delta t j}$, with $n_{\text{terms}} = 10$, amplitudes a_k drawn uniformly from $[0, 1]$ and ℓ_2 -normalized (seed 1001), frequencies ω_k drawn uniformly from $[-20, 20]$ (seed 2002), and decay rates λ_k drawn uniformly from $[-2, 0]$ (seed 4004), ensuring exponential decay; and (iv) a cusp-type signal, $x[j] = |\cos(2\pi j \Delta t)|^{0.8}$, which is non-smooth and used to test robustness against sharp features.

Appendix E: Locating poles and zeros

Although the finite- N transform has no true poles, the pole locations of the corresponding infinite-series can still be estimated from the finite- N data. Here, we consider the signal $x_j \propto a^j \cos(\omega_0 j)$ with $n = 20$, $a \approx 1.00015 e^{i0.002}$ and $\omega_0 = 0.0061$.

We first examine the unit-circle slice ($k = 0$), as shown in Fig. C4. The dominant responses occur at $l = 1364$ and $l = 1047893$, which identify the relevant spectral components. For each of these l -values, we then inspect the corresponding radial slice, shown in Fig. C5. Since the infinite-series transform diverges at the pole, the finite- N signature is not a resolved maximum but the onset of approximate exponential growth, visible as an approximately linear regime on the semilog plot. The corresponding (k, l) values are then used to estimate the pole locations.

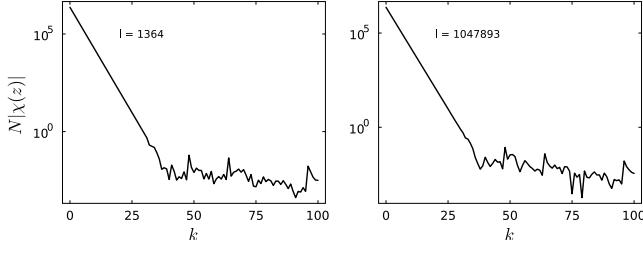


FIG. C5. Radial slices of $N|\chi(z)|$ at $l = 1364$ and $l = 1047893$. The pole is inferred from the onset of divergence-like growth, rather than from a resolved finite- N maximum.

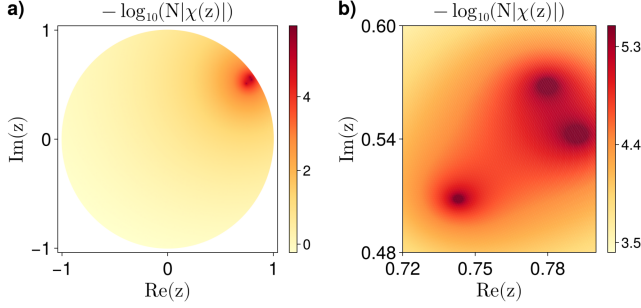


FIG. C6. Zero finding for $X(z) = e^{az}(z - \alpha)(z - \beta)(z - \gamma)$. (a) Coarse scan with $\omega_r = \omega_i = 2\pi$, $\tau = 10^{-15}$, showing the broader z -plane structure and the region containing the zeros. (b) Refined scan with $\omega_r = 0.5$, $\omega_i = 2\pi$, $\tau = 10^{-15}$, near the predicted zero locations, where the three nearby zero locations are inferred as distinct localized maxima in $-\log_{10}(N|\chi(z)|)$.

1. Zero locations

The same approach can also be used to identify zeros of the z -transform. As a test case, we consider

$$X(z) = e^{az}(z - \alpha)(z - \beta)(z - \gamma), \quad (\text{E1})$$

with $\alpha = 0.90 e^{i0.60}$, $\beta = 0.96 e^{i0.60}$, $\gamma = 0.965 e^{i0.63}$, and $a = 0.4$. These zeros are chosen to lie close to one another, in order to test the resolution of our method. For the full analytic function they are exact zeros, while in the finite- N truncated transform they appear numerically as localized minima of $|X(z)|$. As shown in Fig. C6, a coarse scan first identifies the relevant region of the z -plane, after which a refined local scan resolves the three nearby zero locations and estimates their positions as $\alpha = 0.90001 e^{i0.59994}$, $\beta = 0.96010 e^{i0.59993}$, $\gamma = 0.96490 e^{i0.63006}$.